NANO LETTERS

pubs.acs.org/NanoLett

Letter

Spectral- and Polarization-Dependent Scattering of Gold Nanobipyramids for Exogenous Contrast in Optical Coherence Tomography

Pelham Keahey,*[,] Peng Si,[] Mohammad Razavi, Shangjie Yu, Norman Lippok, Martin Villiger, Timothy P. Padera, Adam de la Zerda,* and Brett Bouma

Cite This: *Nano Lett.* 2021, 21, 8595−8601

Read Online

ACCESS | Metrics & More | Article Recommendations | Supporting Information

ABSTRACT: Polarization-sensitive optical coherence tomography (PS-OCT) reveals the subsurface microstructure of biological tissue and provides information regarding the polarization state of light backscattered from tissue. Complementing OCT's structural signal with molecular imaging requires strategies to simultaneously detect multiple exogenous contrast agents with high specificity in tissue. Specific detection of molecular probes enables the parallel visualization of physiological, cellular, and molecular processes. Here we demonstrate that, by combining PS-OCT and spectral contrast (SC)-OCT measurements, we can distinguish signatures of different gold nanobipyramids (GNBPs) in lymphatic vessels from the surrounding tissue and blood vessels in live mouse models. This technique could well be extended to other anisotropic nanoparticle-based OCT contrast agents and presents significant progress toward enabling OCT molecular imaging.

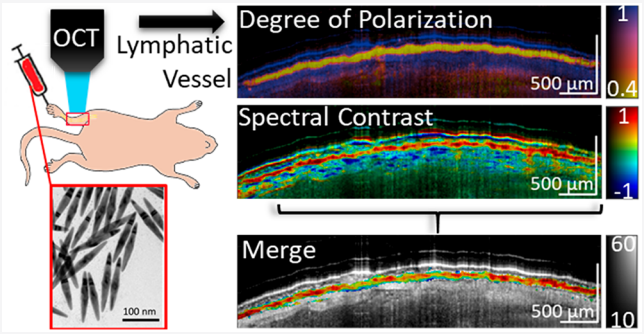

KEYWORDS: *optical coherence tomography, depolarization, contrast agent, lymphatic system, in vivo imaging, gold nanoparticles*

INTRODUCTION

In vivo optical molecular imaging provides visualization of different biomarkers for tracking and mapping of cellular processes and interactions in living tissue. Fluorescent labeling is commonly utilized for multiplexed tracking of many of these biological interactions.[1] However, the conventional detection of widefield epifluorescence is often limited to a few hundreds of micrometers in depth unless advanced multiphoton excitation is used.[2−4] Optical coherence tomography (OCT) reveals the microstructure of biological tissue by measuring the path length difference of backscattered light at a micrometer-scale resolution and with a millimeter-scale depth of penetration.[5] Polarization-sensitive (PS)-OCT further determines the polarization state of the detected light to provide additional information regarding tissue retardation and depolarization.[6] Optical-molecular probes are critical for further enabling the parallel visualization of physiological, cellular, and molecular processes. Unfortunately, most small molecules, antibodies, and fluorescent probes lack intrinsic OCT contrast, as they produce little detectable change in the index of refraction in the second near-infrared window (NIR-II). Developing imaging probes for use with OCT would enable the visualization of biomarkers concurrently with anatomical features at micrometer-scale resolution over wide areas of tissue at several millimeters in depth.

A number of approaches to develop exogenous functional OCT contrast agents have been studied, such as microspheres, high-aspect-ratio nanostructures, magnetic nanoparticles, and plasmonic nanoparticles.[7−14] Plasmonic gold nanostructures have shown promise due to their tunable optical properties and biocompatibility.[15] The unique spectral signatures of plasmonic gold nanostructures have been used for multiplexed OCT imaging *in vivo*.[16−18] However, their detection relied on flow-gating with OCT-angiography (OCTA) to isolate flowing or diffusing particles.[16−19] This allowed for the elimination of artificial spectral signatures induced by speckles in the static background signal. However, the reliance on particle motion significantly restricts labeling strategies and precludes the detection of static particles. In a parallel effort, we recently reported that ensembles of randomly oriented high-aspect-ratio gold nanorods (GNRs) act as a source of depolarization and that this can serve as a detection mechanism of GNRs *in vivo*. However, depolarization lacks a pronounced spectral depend-

Received: June 12, 2021
Revised: October 3, 2021
Published: October 13, 2021

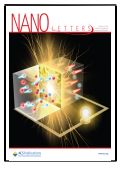

https://doi.org/10.1021/acs.nanolett.1c02291
Nano Lett. 2021, 21, 8595−8601

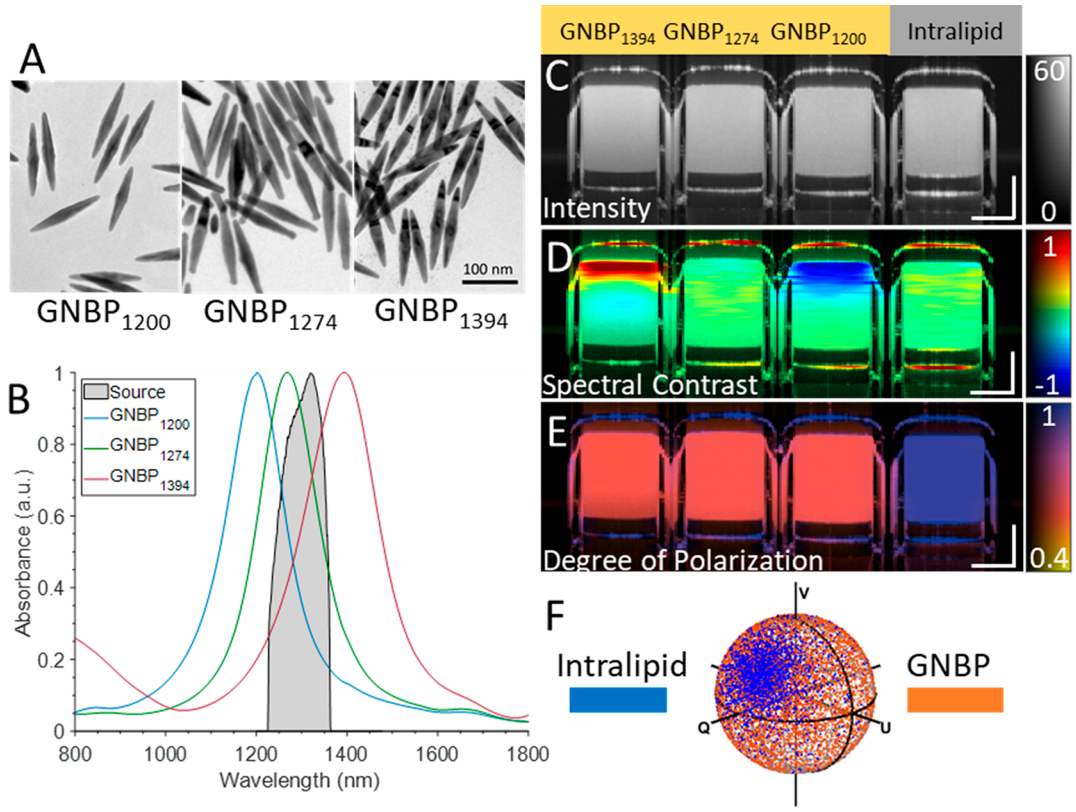

Figure 1. (A) TEM images of GNBPs. (B) Spectra of GNBPs and the PS-OCT system source spectrum. (C) Intensity images $GNBP_{1394}$, $GNBP_{1274}$, $GNBP_{1200}$, and intralipid (left to right). (D) Spectral contrast (SC) and (E) degree of polarization (DOP). (F) Poincare sphere showing raw Stokes vectors of nondepolarizing intralipid vs depolarizing GNBPs. Scale bars: 250 μm. SC color scale: −1 to 1. DOP: 0.4 to 1. The intensity is on the dB scale.

ence and does not allow for multiplexing.[20] To address the need for multiplexed and specific detection of exogenous labels in scattering tissue, here we combine depolarization and spectral measurements to achieve a versatile and specific image contrast for gold nanoparticles with PS-OCT.

In this study, we first characterize the depolarization and spectral signatures of gold nanobipyramids (GNBPs) using a wavelength swept-source PS-OCT system in a series of *in vitro* experiments. We then show that depolarization and spectral measurements can be used to visualize subcutaneous injections of GNBPs for multiplexed mapping of lymphatic vessels *in vivo* and enable identification of static GNBPs collected in associated draining lymph nodes.

RESULTS AND DISCUSSION

***In Vitro* Characterization of Depolarization and Spectral Contrast Signals.** Gold nanobipyramids were prepared according to the method described in the Supporting Information and by Si et al.[18] The synthesized GNBPs were imaged using transmission electron microscopy (Figure 1A). Three different kinds of GNBPs were synthesized with plasmonic resonances at 1200, 1274, and 1394 nm, allowing portions of their spectra to overlap with the spectral band of NIR-II wavelength swept-source PS-OCT systems (Figure 1B). GNBPs were chosen due to their narrower plasmonic bandwidth in comparison to gold nanorods.[18] Throughout this work a wavelength swept-source PS-OCT system was used with a source central wavelength of 1310 nm and with an approximate axial resolution of 10 μm and a lateral resolution of 20 μm. To demonstrate depolarization and spectral contrast (SC) measurements of GNBPs, four capillary tubes containing a control (intralipid 1%) and three different 500 pM GNBP solutions were imaged. Intralipid was used as a control due to its common use as an OCT contrast agent and its lack of significant intrinsic spectral or polarization characteristics.[21] Intensity images of the capillary tubes reveal similar scattering signals among the samples (Figure 1C). Next, the spectral contrast was computed using a dual-band spectral analysis algorithm.[17,18,22] In brief, the algorithm computes two OCT interferograms utilizing the halves of the source spectral bandwidth. Computational corrections for dispersion, rolloff, and source power imbalance were applied to both bands. Afterward, the intensity tomogram originating from the shorter wavelength half was subtracted from the longer wavelength tomogram to reveal spectral differences in the scattering signal. Enhanced scattering at longer wavelengths of the PS-OCT spectrum results in positive (red) spectral contrast, while enhanced scattering in the shorter half results in negative (blue) spectral contrast. $GNBP_{1200}$ and $GNBP_{1394}$ exhibit negative and positive contrast, respectively (Figure 1D). Alternatively, intralipid and $GNBP_{1274}$ exhibit neutral spectral contrast, as scattering is approximately equal across the halves of the source spectrum (Figure 1D). Both $GNBP_{1200}$ and $GNBP_{1394}$ exhibit an apparent neutralizing spectral contrast signal with depth as a result of particle absorption, previously referred to as spectral shadowing.[18] Prior to this study, to the best of our knowledge, only high-aspect-ratio GNRs had been demonstrated to exhibit depolarization that could be used as a contrast mechanism for PS-OCT.[20] A numerical analysis revealed similar polarization-dependent scattering cross

https://doi.org/10.1021/acs.nanolett.1c02291
Nano Lett. 2021, 21, 8595−8601

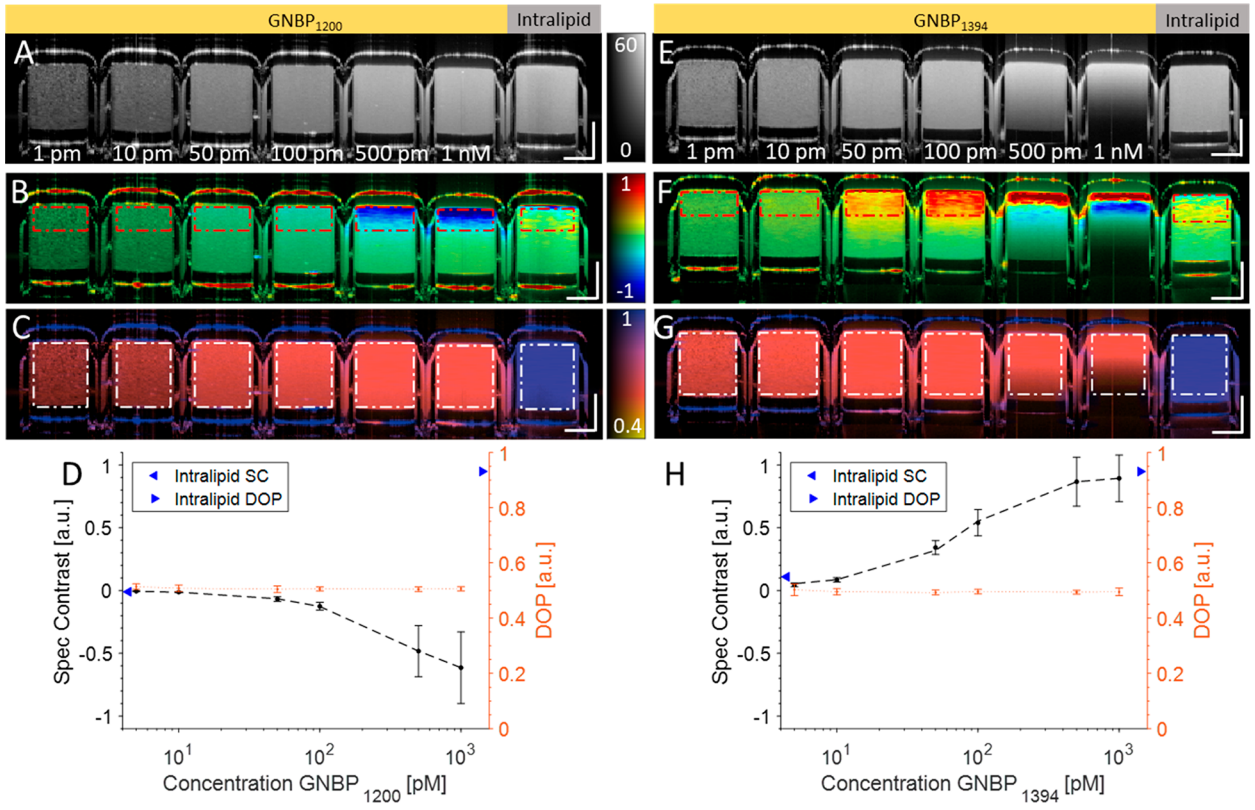

Figure 2. (A) Intensity, (B) spectral contrast, and (C) DOP of a dilution series of $GNBP_{1200}$ (1 nM, 500 pM, 100 pM, 50 pM, 10 pM, and 1 pM) and 1% intralipid control. (D) Quantification of spectral contrast and DOP exhibited by the control and $GNBP_{1200}$ within the red and white ROIs, respectively. (E–G) Intensity, spectral contrast, and DOP of $GNBP_{1394}$ and 1% intralipid. (H) Quantification of spectral contrast and DOP from $GNBP_{1394}$ within the red and white ROIs, respectively. Scale bars: 250 μm. The intensity is on the dB scale. SC color scale: −1 to 1. DOP: 0.4 to 1.

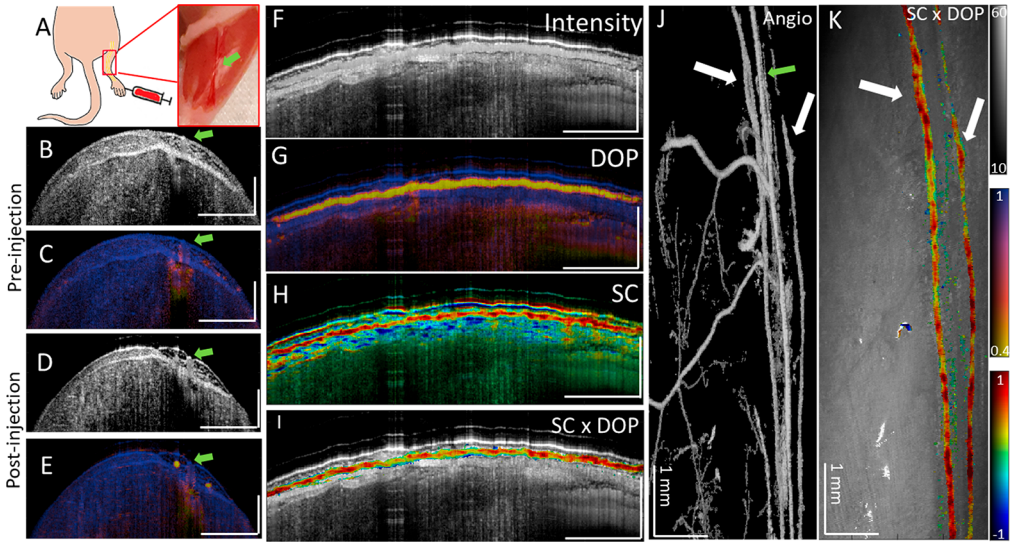

Figure 3. (A) Schematic and photograph of imaging area on the hind limb after skin removal. (B, C) Intensity and DOP cross-section of the hind leg prior to $GNBP_{1394}$ injection. (D, E) Intensity and DOP cross-section of the hind leg after to $GNBP_{1394}$ injection. Lymphatic vessels (yellow) can be seen in (E). Longitudinal views of (F) intensity, (G) DOP, and (H) spectral contrast of the left lymphatic vessel. Note the negatively contrasting spectral shadow below most of the length of the positively contrasting lymphatic vessel. (I) Spectral contrast (SC) masked using DOP and overlaid onto the intensity image. (J) Enface intensity masked by angiography and (K) enface view of the tissue surface with masked spectral contrast. The green arrow identifies the saphenous vein. White arrows show low DOP the signal with the corresponding angiography signal, identifying lymphatic vessels. Unless otherwise noted, the horizontal scale bar is 1 mm and the vertical bar is 500 μm. The intensity is given on the dB scale. SC color scale: −1 to 1. DOP: 0.4 to 1.

sections of GNBPs and GNRs near the longitudinal resonance wavelength (Figure S1). To confirm this experimentally, we quantified depolarization or polarization state scrambling using degree of polarization (DOP) measurements with PS-OCT.[20,23] DOP quantifies the uniformity of polarization states expressed as Stokes vectors in a small spatial neighborhood of a

https://doi.org/10.1021/acs.nanolett.1c02291
Nano Lett. 2021, 21, 8595−8601

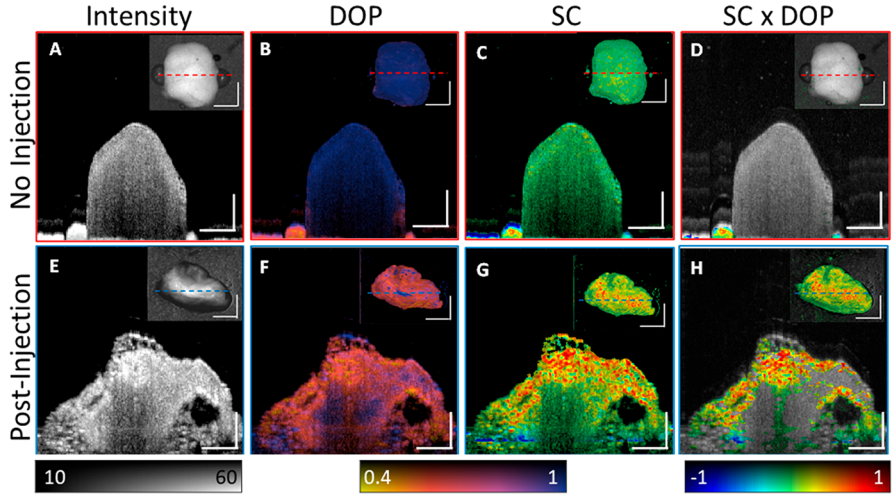

Figure 4. Resected popliteal lymph nodes. (A–D) Popliteal lymph node from a control mouse without any injection of GNBPs. Cross-section images of (A) intensity, (B) DOP, (C) spectral contrast, and (D) spectral contrast gated using DOP. (E–H) Popliteal lymph node from a mouse after $GNBP_{1394}$ injection. Cross-section images of (E) intensity, (F) DOP, (G) spectral contrast, and (H) spectral contrast gated using DOP. DOP gating ignored pixels with DOP > 0.7 and SNR< 15 dB. Inset images are enface projection images. The dotted lines indicate the position of the cross-section plane. Scale bars: 0.5 mm. The intensity is given on the dB scale. SC color scale: −1 to 1.

PS-OCT tomogram. DOP is in the range of 1 (completely polarized) to 0 (completely depolarized), where the polarization states have a high degree of randomness. The experimental results revealed that each GNBP exhibited a strong depolarization signature visualized by a loss of DOP (Figure 1E,F). Additionally, DOP measurements enable differentiation of the neutrally contrasting intralipid control from neutrally contrasting $GNBP_{1274}$.

We then imaged a dilution series of $GNBP_{1200}$ and $GNBP_{1394}$ suspended in water along with an intralipid control (Figure 2). The full spectrum intensity visibly increases as the concentration increases from 1 pM to 1 nM for both $GNBP_{1200}$ and $GNBP_{1394}$ (Figure 2A,E). $GNBP_{1200}$ shows a negative spectral contrast due to enhanced scattering in the shorter wavelength band, while $GNBP_{1394}$ exhibits positive spectral contrast due to enhanced scattering in the longer wavelength band (Figure 2B,F). Converse to scattering, GNBP absorption is also enhanced in their respective wavelength bands. Absorption-driven spectral contrast can result in an oppositely contrasting signal in comparison to scattering-driven contrast. The transition between scattering- and absorption-driven spectral contrast can most prominently be observed in Figure 2F at the 1 nM concentration. Here a strong scattering-based positive spectral contrast signal from $GNBP_{1394}$ can be observed at the surface. However, this positive contrast signal becomes neutralized and eventually strongly negative at greater depths due to enhanced abortion (decreased signal) in the longer-wavelength band. For quantitative analysis, regions of interest (ROIs) were defined at the top of the tubes to avoid absorption-driven contrast effects. Additionally, both GNBP particles exhibited strong depolarization for all concentrations, while the intralipid control exhibited little loss (blue) of DOP (Figure 2D,H). In these GNBP suspensions, meaningful NIR-II scattering was only from depolarizing GNBPs; thus, all detected light should be depolarized and have a lowered DOP. Conversely, when GNBPs were mixed with nondepolarizing scatterers, such as whole blood, DOP does have a concentration dependence (Figure S2).

***In Vivo* Detection of Depolarization and Spectral Signatures.** For *in vivo* experiments, GNBPs were PEGylated (PEG, MW ≈ 5 kDa) for stability and biocompatibility purposes. To first validate particle isolation using depolarization and identification using spectral contrast, we imaged passive accumulation of $GNBP_{1394}$ in mouse hindlimb lymphatic vessels *in vivo* after subcutaneous injection into the foot (Figure 3A). GNBP particles used in this study were larger than 100 nm and should predominantly enter the lymphatics, as they are too large for reabsorption into blood capillaries.[24] However, unlike blood, lymph minimally scatters NIR light and assessment without exogenous contrast is challenging using PS-OCT. To demonstrate, we imaged along the saphenous vein of a mouse leg before the injection of $GNBP_{1394}$ (Figure 3B,C and and Figure S3). Cross-sectional intensity and DOP images of the hind leg prior to injection of 6 nM $GNBP_{1394}$ (Figure S4) show no apparent lymphatic vessels or loss of DOP on either side of the saphenous vein indicated by the green arrow (Figure 3A–C). After injection of 1 uL of 6 nM $GNBP_{1394}$ subcutaneously into the foot, a clear loss of DOP (in yellow) becomes visible in two vessels (Figure 3D,E). Longitudinal segmentation tracking the left lymph vessel reveals a clear intensity signal and loss of DOP along its length (Figure 3F,G). The spectral contrast shows a strong positive contrast along the length of the lymphatic vessel together with spectral noise and a strong negatively contrasting spectral shadow below the vessel (Figure 3H). The recorded volume was then segmented by masking pixels with high DOP (DOP > 0.7) and low signal levels (SNR < 20 dB). After masking, the spectral contrast was overlaid onto the longitudinal intensity, revealing a clear positive contrast signal along the length of the lymphatic vessel, consistent with the injection of $GNBP_{1394}$ (Figure 3I). Additionally, an enface image using OCTA visualized the signal from blood flow and the two lymph vessels containing $GNBP_{1394}$ indicated by white arrows (Figure 3J). Using DOP segmentation, an enface SC × DOP image is displayed where both lymph vessels show positive contrast (Figure 3K). To further confirm $GNBP_{1394}$ uptake into the lymphatic vessels in the mouse leg, the popliteal lymph node was resected (n = 3) and imaged *ex vivo* (Figure 4). Without GNBP injection, popliteal lymph nodes show little depolarization or significant spectral contrast

https://doi.org/10.1021/acs.nanolett.1c02291
Nano Lett. 2021, 21, 8595−8601

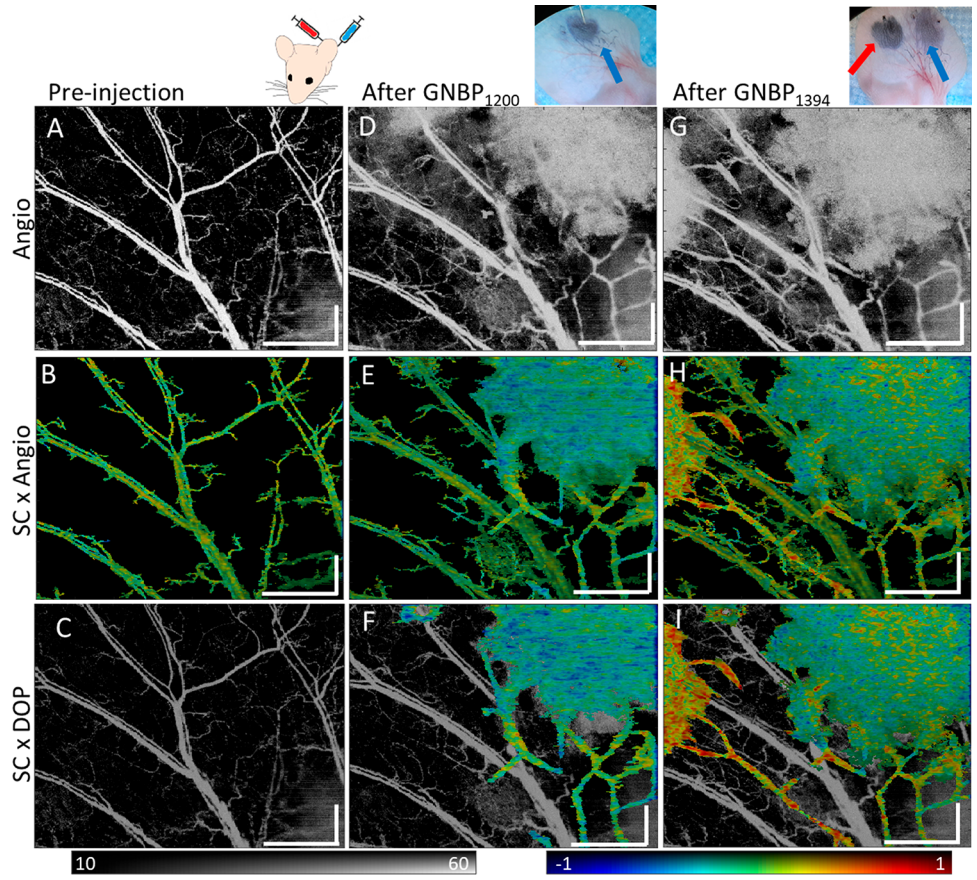

Figure 5. Sequential GNBP injection into mouse ear. (A) Angiography image of a mouse ear prior to GNBP injection. (B) Spectral contrast masked using angiography. (C) Spectral contrast masked using DOP masking overlaid onto the dimmed angiography image for reference. No significant DOP loss wasobserved prior to injection. (D) Angiography after $GNBP_{1200}$ injection showing the first injection site in the upper right. (E) Spectral contrast masked using angiography and (F) spectral contrast masked using DOP overlaid onto the dimmed angiography image. (G) Angiography after $GNBP_{1394}$ injection on the left side of the ear. (H) Spectral contrast masked using angiography and (I) spectral contrast masked using DOP overlaid onto the dimmed angiography image. Scale bars: 1 mm. The intensity is given on the dB scale. SC color scale: −1 to 1.

(Figure 4A–D). After $GNBP_{1394}$ injection, significant loss of DOP is observed throughout the popliteal lymph node along with a strong positive contrast consistent with the signal observed in the leg (Figure 4D–G).

***In Vivo* Multiplexing.** To image two contrasting GNBPs simultaneously *in vivo*, we subcutaneously injected 1.0 μL of 6 nM PEGylated $GNBP_{1200}$ and $GNBP_{1394}$ at two separate locations sequentially into the ear of a mouse. Due to the GNBP size, particles will be preferentially taken up by lymphatic vessels. PS-OCT volumetric scans of the ear were taken prior to injection of both particles (Figure 5A–C). Enface projections of angiography prior to injection of particles are shown (Figure 5A). Spectrally neutral blood vessels can be observed (Figure 5B), and no vessels exhibit significant DOP loss (Figure 5C). Upon injection of $GNBP_{1200}$, we observed an enhanced angiography signal at the $GNBP_{1200}$ injection site and a new signal from presumably lymphatic vessels predominantly in the lower right quadrant (Figure 5D). Angiography was then used to segment the spectral contrast but without prior knowledge does not differentiate between blood flow and lymph flow (Figure 5E). Although negative contrast is visible from the $GNBP_{1200}$ injection, some areas of the lymphatic vessel still appear neutral due to variations in concentrations of GNBP in the vessels. After DOP segmentation, lymphatic vessels containing GNBPs can be clearly differentiated from blood vessels, which only showed an angiographic signal (Figure 5F). After $GNBP_{1394}$ injection in a different location, additional lymphatic vessels draining that area of skin become visible in angiography (Figure 5G). The angiography signal and positive spectral contrast signal were then observed at the left injection site (Figure 5H). DOP differentiates GNBPs in lymphatic vessels from confounding blood flow (Figure 5I). Here we were able to show clear differentiation between blood flow and GNBP particle uptake in lymphatic vessels by using depolarization and spectral signatures.

CONCLUSIONS

We have shown that the combination of depolarization and spectral measurements enables a contrast enhancement of multiplexed, exogenous labels with PS-OCT. Utilizing depolarization, we demonstrated that GNBP locations can be differentiated from the surrounding highly scattering tissue. Spectral measurements of isolated GNBPs can be used to identify GNBPs with differing plasmonic resonances. In combination, this detection scheme offers a platform for direct detection and differentiation of nanoparticles within highly scattering tissue. Furthermore, depolarization and spectral-based detection uniquely enables differentiation of neutrally contrasting particles, such as $GNBP_{1274}$, from other spectrally neutral nondiattenuating sources. Scattering from GNBPs in lymphatic vessels can also be differentiated from moving

https://doi.org/10.1021/acs.nanolett.1c02291
Nano Lett. 2021, 21, 8595−8601

scatterers in blood vessels to better separate lymphatic and blood vessel scattering without the need for manual segmentation.[18,25]

One area of possible interreference of GNBP detection using depolarization is endogenous depolarizing structures such as the retinal pigment epithelium (RPE), optic nerve head, and arterial plaques. Additional image segmentation would be required in the presence of such depolarizing structures or others.[26,27] However, unlike other molecular imaging techniques, this scattering-based method has the advantage of not being hindered by photobleaching, quenching, or autofluorescence. In comparison with previously reported OCT spectral contrast techniques,[18] this polarization-dependent spectral contrast method enables the specific detection of multiple nanoparticles simultaneously both inside and outside the vascular system, providing prospects for a wide range of biological applications.

The novel detection and multiplexing technique we report here provides a platform for *in vivo* imaging studies using PS-OCT. This technique opens up many opportunities for *in vivo* optical molecular imaging and can provide visualization of multiple contrast agents simultaneously at micrometer-scale resolution and millimeter scales of depth. For lymphatic research, our technique could be used to map lymphangiogenesis in tumors, an important factor in cancer progression and immunotherapy. Lymph node metastasis has profound clinical significance, and this technique could be employed for sentinel lymph nodes or lymphangiogenesis biomarkers.[28] This technique could also enable further study of the role of the lymphatic system in the brain and its relation to neurodegenerative disease.

MATERIALS AND METHODS

Complete details of methods for nanoparticle synthesis, instrumentation, image processing, and *in vitro* and *in vivo* experiments are provided in the Supporting Information.

ASSOCIATED CONTENT

Supporting Information

The Supporting Information is available free of charge at https://pubs.acs.org/doi/10.1021/acs.nanolett.1c02291.

> Preparation of gold nanobipyramids, optical coherence tomography imaging system specifications, spectral contrast and depolarization image processing, *in vitro* imaging experimental methods, *in vivo* animal imaging and handling methods, electromagnetic simulations of gold nanobipyramids, simulated scattering of GNBPs from 400 to 1600 nm, signal from GNBP dilutions mixed with human whole blood, *in vivo* mouse leg pre- and postinjection of GNBPs control image, *in vitro* comparison of depolarization and spectral contrast of 6 nM vs 1 nM GNBP, and evaluation of cellular uptake of GNBPs (PDF)

AUTHOR INFORMATION

Corresponding Authors

Pelham Keahey − *Wellman Center for Photomedicine, Massachusetts General Hospital, Boston, Massachusetts 02114, United States; Harvard Medical School, Boston, Massachusetts 02115, United States;* orcid.org/0000-0002-9504-9696; Email: pkeahey@mgh.harvard.edu

Adam de la Zerda − *Department of Structural Biology, Stanford University, Stanford, California 94305, United States; Molecular Imaging Program at Stanford, Stanford, California 94305, United States; Department of Electrical Engineering, Stanford University, Stanford, California 94305, United States; Biophysics Program at Stanford, Stanford, California 94305, United States; The Bio-X Program, Stanford, California 94305, United States; The Chan Zuckerberg Biohub, San Francisco, California 94158, United States*; Email: adlz@stanford.edu

Authors

Peng Si − *Department of Structural Biology, Stanford University, Stanford, California 94305, United States; Molecular Imaging Program at Stanford, Stanford, California 94305, United States;* orcid.org/0000-0003-2596-8360

Mohammad Razavi − *Harvard Medical School, Boston, Massachusetts 02115, United States; Edwin L. Steele Laboratories, Department of Radiation Oncology, Massachusetts General Hospital, Boston, Massachusetts 02114, United States*

Shangjie Yu − *Department of Electrical Engineering, Stanford University, Stanford, California 94305, United States;* orcid.org/0000-0002-5507-8425

Norman Lippok − *Wellman Center for Photomedicine, Massachusetts General Hospital, Boston, Massachusetts 02114, United States; Harvard Medical School, Boston, Massachusetts 02115, United States*

Martin Villiger − *Wellman Center for Photomedicine, Massachusetts General Hospital, Boston, Massachusetts 02114, United States; Harvard Medical School, Boston, Massachusetts 02115, United States*

Timothy P. Padera − *Harvard Medical School, Boston, Massachusetts 02115, United States; Edwin L. Steele Laboratories, Department of Radiation Oncology, Massachusetts General Hospital, Boston, Massachusetts 02114, United States*

Brett Bouma − *Wellman Center for Photomedicine, Massachusetts General Hospital, Boston, Massachusetts 02114, United States; Harvard Medical School, Boston, Massachusetts 02115, United States; Institute for Medical Engineering and Science, Massachusetts Institute of Technology, Cambridge, Massachusetts 02139, United States*

Complete contact information is available at: https://pubs.acs.org/10.1021/acs.nanolett.1c02291

Author Contributions

■P.K. and P.S. contributed equally.

Author Contributions

P.K. and P.S. designed the experiments, P.K,. P.S., and M.R. performed the experiments, P.K., P.S., and S.Y. wrote the code for image processing and data analysis. All authors analyzed the data. P.K., P.S., M.V., T.P.P., A.d.l.Z., and B.B. wrote the manuscript with contributions from all authors.

Notes

The authors declare no competing financial interest.

ACKNOWLEDGMENTS

The authors would like to thank Taylor Cannon for assistance with *in vitro* experiments and Dr. Pinji Lei for help with animal imaging. The work was funded by grant number P41EB015903 awarded by the National Institute of Biomedical Imaging and

Bioengineering anda Grant No. 5F99CA212217-02 F99/K00 fellowship awarded by the National Cancer Institute of the National Institutes of Health. Further support was provided by NIH R01CA214913 (T.P.P.), MGH Research Scholars Program (T.P.P.), NIH F32HL156654 (M.R.), the Claire Giannini Fund, the National Institutes of Health (NIH DP50D012179), the Damon Runyon Cancer Research Foundation (DFS#06-13), the Donald E. and Delia B. Baxter Foundation, and the Skippy Frank Foundation. A.d.l.Z. is a Chan Zuckerberg Biohub investigator and a Pew-Stewart Scholar for Cancer Research supported by The Pew Charitable Trusts and The Alexander and Margaret Stewart Trust.

REFERENCES

(1) Hellebust, A.; Richards-Kortum, R. Advances in Molecular Imaging: Targeted Optical Contrast Agents for Cancer Diagnostics. *Nanomedicine* **2012**, *7* (3), 429−445.
(2) Ntziachristos, V. Going Deeper than Microscopy: The Optical Imaging Frontier in Biology. *Nat. Methods* **2010**, *7* (8), 603−614.
(3) Yun, S. H.; Tearney, G. J.; Vakoc, B. J.; Shishkov, M.; Oh, W. Y.; Desjardins, A. E.; Suter, M. J.; Chan, R. C.; Evans, J. A.; Jang, I.; Nishioka, N. S.; de Boer, J. F.; Bouma, B. E. Comprehensive Volumetric Optical Microscopy in Vivo. *Nat. Med.* **2006**, *12* (12), 1429−1433.
(4) Liu, H.; Deng, X.; Tong, S.; He, C.; Cheng, H.; Zhuang, Z.; Gan, M.; Li, J.; Xie, W.; Qiu, P.; Wang, K. In Vivo Deep-Brain Structural and Hemodynamic Multiphoton Microscopy Enabled by Quantum Dots. *Nano Lett.* **2019**, *19* (8), 5260−5265.
(5) Huang, D.; Swanson, E. A.; Lin, C. P.; Schuman, J. S.; Stinson, W. G.; Chang, W.; Hee, M. R.; Flotte, T.; Gregory, K.; Puliafito, C. A.; Fujimoto, J. G. Optical Coherence Tomography. *Science* **1991**, *254* (5035), 1178−1181.
(6) Hee, M. R.; Swanson, E. A.; Fujimoto, J. G.; Huang, D. Polarization-Sensitive Low-Coherence Reflectometer for Birefringence Characterization and Ranging. *J. Opt. Soc. Am. B* **1992**, *9* (6), 903.
(7) Lee, T. M.; Oldenburg, A. L.; Sitafalwalla, S.; Marks, D. L.; Luo, W.; Toublan, F. J.-J.; Suslick, K. S.; Boppart, S. A. Engineered Microsphere Contrast Agents for Optical Coherence Tomography. *Opt. Lett.* **2003**, *28* (17), 1546.
(8) John, R.; Rezaeipoor, R.; Adie, S. G.; Chaney, E. J.; Oldenburg, A. L.; Marjanovic, M.; Haldar, J. P.; Sutton, B. P.; Boppart, S. A. In Vivo Magnetomotive Optical Molecular Imaging Using Targeted Magnetic Nanoprobes. *Proc. Natl. Acad. Sci. U. S. A.* **2010**, *107* (18), 8085−8090.
(9) Agrawal, A.; Huang, S.; Wei Haw Lin, A.; Lee, M.-H.; Barton, J. K.; Drezek, R. A.; Pfefer, T. J. Quantitative Evaluation of Optical Coherence Tomography Signal Enhancement with Gold Nanoshells. *J. Biomed. Opt.* **2006**, *11* (4), 041121.
(10) Jung, Y.; Reif, R.; Zeng, Y.; Wang, R. K. Three-Dimensional High-Resolution Imaging of Gold Nanorods Uptake in Sentinel Lymph Nodes. *Nano Lett.* **2011**, *11* (7), 2938−2943.
(11) Oldenburg, A. L.; Crecea, V.; Rinne, S. A.; Boppart, S. A. Phase-Resolved Magnetomotive OCT for Imaging Nanomolar Concentrations of Magnetic Nanoparticles in Tissues. *Opt. Express* **2008**, *16* (15), 11525−11539.
(12) Tucker-Schwartz, J. M.; Beavers, K. R.; Sit, W. W.; Shah, A. T.; Duvall, C. L.; Skala, M. C. In Vivo Imaging of Nanoparticle Delivery and Tumor Microvasculature with Multimodal Optical Coherence Tomography. *Biomed. Opt. Express* **2014**, *5* (6), 1731.
(13) Lapierre-Landry, M.; Gordon, A. Y.; Penn, J. S.; Skala, M. C. In Vivo Photothermal Optical Coherence Tomography of Endogenous and Exogenous Contrast Agents in the Eye. *Sci. Rep.* **2017**, *7* (1), 9228.
(14) Xu, Y.; Zhou, B.; Zhuang, C.; Zhou, J.; Chen, H.; Deng, S. High-Aspect-Ratio Plasmonic Heterostructures for In Vivo Enhanced Optical Coherence Tomography Imaging in the Second Near-Infrared Biological Window. *Adv. Opt. Mater.* **2020**, *8* (15), 2000384.
(15) Dreaden, E. C.; Alkilany, A. M.; Huang, X.; Murphy, C. J.; El-Sayed, M. A. The Golden Age: Gold Nanoparticles for Biomedicine. *Chem. Soc. Rev.* **2012**, *41* (7), 2740−2779.
(16) Si, P.; Yuan, E.; Liba, O.; Winetraub, Y.; Yousefi, S.; Sorelle, E. D.; Yecies, D. W.; Dutta, R.; De La Zerda, A. Gold Nanoprisms as Optical Coherence Tomography Contrast Agents in the Second Near-Infrared Window for Enhanced Angiography in Live Animals. *ACS Nano* **2018**, *12* (12), 11986−11994.
(17) Liba, O.; Sorelle, E. D.; Sen, D.; De La Zerda, A. Contrast-Enhanced Optical Coherence Tomography with Picomolar Sensitivity for Functional in Vivo Imaging. *Sci. Rep.* **2016**, *6* (1), 1−12.
(18) Si, P.; Shevidi, S.; Yuan, E.; Yuan, K.; Lautman, Z.; Jeffrey, S. S.; Sledge, G. W.; de la Zerda, A. Gold Nanobipyramids as Second Near Infrared Optical Coherence Tomography Contrast Agents for in Vivo Multiplexing Studies. *Nano Lett.* **2020**, *20* (1), 101−108.
(19) Chhetri, R. K.; Blackmon, R. L.; Wu, W. C.; Hill, D. B.; Button, B.; Casbas-Hernandez, P.; Troester, M. A.; Tracy, J. B.; Oldenburg, A. L.; Yang, C. Probing Biological Nanotopology via Diffusion of Weakly Constrained Plasmonic Nanorods with Optical Coherence Tomography. *Proc. Natl. Acad. Sci. U. S. A.* **2014**, *111* (41), E4289−E4297.
(20) Lippok, N.; Villiger, M.; Albanese, A.; Meijer, E. F. J.; Chung, K.; Padera, T. P.; Bhatia, S. N.; Bouma, B. E. Depolarization Signatures Map Gold Nanorods within Biological Tissue. *Nat. Photonics* **2017**, *11* (9), 583−588.
(21) Si, P.; Honkala, A.; de la Zerda, A.; Smith, B. R. Optical Microscopy and Coherence Tomography of Cancer in Living Subjects. *Trends in Cancer* **2020**, *6* (3), 205−222.
(22) Villiger, M.; Zhang, E. Z.; Nadkarni, S. K.; Oh, W.-Y.; Vakoc, B. J.; Bouma, B. E. Spectral Binning for Mitigation of Polarization Mode Dispersion Artifacts in Catheter-Based Optical Frequency Domain Imaging. *Opt. Express* **2013**, *21* (14), 16353.
(23) Lippok, N.; Villiger, M.; Bouma, B. E. Degree of Polarization (Uniformity) and Depolarization Index: Unambiguous Depolarization Contrast for Optical Coherence Tomography. *Opt. Lett.* **2015**, *40* (17), 3954−3957.
(24) Swartz, M. The Physiology of the Lymphatic System. *Adv. Drug Delivery Rev.* **2001**, *50* (1−2), 3−20.
(25) Liba, O.; SoRelle, E. D.; Sen, D.; de la Zerda, A. Contrast-Enhanced Optical Coherence Tomography with Picomolar Sensitivity for Functional in Vivo Imaging. *Sci. Rep.* **2016**, *6* (1), 23337.
(26) Ahlers, C.; Götzinger, E.; Pircher, M.; Golbaz, I.; Prager, F.; Schütze, C.; Baumann, B.; Hitzenberger, C. K. Imaging of the Retinal Pigment Epithelium in Age-Related Macular Degeneration Using Polarization-Sensitive Optical Coherence Tomography. *Invest. Ophthalmol. Visual Sci.* **2010**, *51* (4), 2149−2157.
(27) Villiger, M.; Otsuka, K.; Karanasos, A.; Doradla, P.; Ren, J.; Lippok, N.; Shishkov, M.; Daemen, J.; Diletti, R.; van Geuns, R.-J.; Zijlstra, F.; van Soest, G.; Libby, P.; Regar, E.; Nadkarni, S. K.; Bouma, B. E. Coronary Plaque Microstructure and Composition Modify Optical Polarization. *JACC Cardiovasc. Imaging* **2018**, *11* (11), 1666−1676.
(28) Padera, T. P.; Meijer, E. F. J.; Munn, L. L. The Lymphatic System in Disease Processes and Cancer Progression. *Annu. Rev. Biomed. Eng.* **2016**, *18* (1), 125−158.

https://doi.org/10.1021/acs.nanolett.1c02291
Nano Lett. 2021, 21, 8595−8601